APPLICATION OF SQUEEZE FILM DAMPERS

Edoardo Gheller [0000-0003-4381-3135], and Steven Chatterton [0000-0003-4170-009X], Andrea Vania [0000-0001-8277-1498] and Paolo Pennacchi [0000-0001-8174-0462]

Dept. of Mechanical Engineering, Politecnico di Milano
Via G. la Masa 1, 20156 Milan, Italy
{edoardo.gheller, steven.chatterton, andrea.vaia}
paolo.pennacchi@polimi.it

Abstract. The level of the vibrations and the presence of instability are the two most critical aspects regarding the operations of turbomachinery. To cope with this issues that may compromise the operation of the machines, squeeze film dampers (SFD) are often used in many industrial applications. Unfortunately, many complex phenomena characterize the dynamic behavior of these components and determine the high complexity of the modeling of these components. The most relevant phenomena involved in the characterization of SFDs are individuated after a comprehensive investigation of the state of the art. Among them, the oil film cavitation, the air ingestion, and the effect of the inertia are introduced. A modeling strategy based on the Reynolds equation is then presented. The boundary conditions to be adopted for the feeding and discharging of oil are investigated and implemented. Eventually, the finite difference model is applied to a practical example to evaluate the possibility to minimize the vibration level and to reduce the effect of the instability if a SFD is added to a rotordynamic system. Meaningful information about the modeling of SFDs is provided in this work. The critical aspects of these components and their modeling are highlighted and discussed.

Keywords: Squeeze Film Damper, Instability, Vibrations.

1 Introduction

In mechanical engineering high levels of vibrations are problematic in all fields, especially in rotordynamics. To increase the productivity and the efficiency of rotating machines, the load that applied to these mechanical components are becoming more and more remarkable. Also considering the increase of the operation speeds, to guarantee safe long operation times is fundamental to reduce the vibrations. In rotordynamics, the typical problems to be dealt with are the high levels of steady state synchronous vibration and the subsynchronous rotor instabilities. The first one is usually dependent on excessive unbalance or if the machine is operated close to a critical speed. On the contrary, the second one is linked to the presence of some instability sources, connected to cross-coupling effects arising, for example, in bearings or seals. Moreover, the level of the vibration when a critical speed is crossed during a runup, or a rundown may also be detrimental to the operation of the machine. Given these considerations, the dynamic

response of the system should benefit from the addition of damping. When the system is supported by rolling element bearings, the damping introduced in the system may be insufficient. Therefore, squeeze film dampers (SFDs can be considered to this aim. Both the dissipation of the vibrational energy and the improvement of the dynamic stability of the rotor-bearing system can be improved by these components.

The most widespread design for such components is the one coupled with rolling element bearings, as shown in **Fig. 1**.
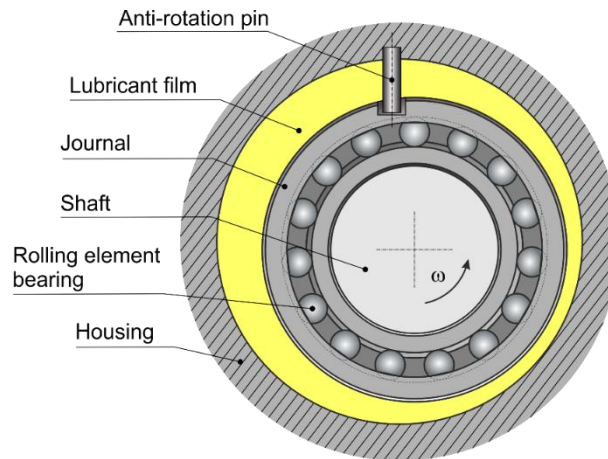

Fig. 1. SFD schematization.

A rolling element bearing supports the shaft. The coupling of the two elements is often referred as journal. The external ring of the bearing moves together with the shaft and the lubricant film, placed between the external surface of the journal and the housing, is "squeezed". The damping effect is generated by the large dynamic forces generated by the large dynamic pressures generated by the squeeze. An anti-rotation pin may be adopted to avoid the transmission of the spinning motion from the shaft to the oil. Only lateral displacement is possible. In other words, the journal cannot spin around its axis of symmetry but only translate. The bearing presence determines the decoupling of the journal motion from the shaft spinning. The shaft kinematics are explained more in the detail in Section 2.1.

Most of the times, supports are applied to sustain the journal at the runup until the vibration amplitude is high enough to guarantee the detachment between the casing and the journal. Therefore, a supporting structure, such as O-rings and squirrel cages, is applied to reduce the risk of impacts. Then they avoid the presence of strong non-linearity determined by the detachment of the journal from the casing. The stiffness of the supporting structure is indeed one fundamental parameter for the optimal operation of the SFD. If the stiffness of the supporting structure is over dimensioned, the relative motion between the journal and the cage will be limited reducing the squeezing of the lubricant film. On the contrary, if the supporting structure is not stiff enough, the SFD can behave as a non-supported one and may be subject to impacts and damages, [1, 2].

SFDs are designed to introduce in the system the optimal level of damping that is strongly dependent on the application. For example, SFDs characterized by lower damping may reduce more the amplitude of the than the ones characterized by higher damping.

The ideal level of damping needed by a machine generally depends on the type of the excitations, the operating conditions, and the dynamic characteristics of the system [3, 4]. In the literature, the modeling of the dynamic behavior of SFDs is performed with numerous models characterized by distinct levels of complexity. The 1D Reynolds equation was the first one considered for SFDs with length to diameter ratios lower than 0.25 and if no sealing mechanism is adopted, [5]. Linearized stiffness and damping coefficients are adopted. However, if the spinning motion is not considered, no stiffness is introduced in the system by the SFD. When the hypothesis of infinitely long bearing is valid, another form of the 1D Reynolds equation is adopted [5]. For both approximations, the resulting equations can be analytically solved, and numerous examples of force coefficients may be found, [2, 3].

The shaft motion needs to be modeled to characterize the dynamic behavior of SFDs. Two different approaches can be followed: circular synchronous orbits, centered or with a statically eccentric, or small amplitude motions about a static displaced center. The first one is usually considered to investigate the response to unbalance, while the second one is considered to analyze the stability of the system, [6].

The SFD clearance and length to diameter ration results as fundamental parameters to characterize the operation of the SFD depending on the level of the vibration, [1–3]. The simplicity is the main advantage of the models based on the 1-D Reynolds equation but, unfortunately, the resulting predictions are accurate only for a reduced range of operating conditions and for simplified geometrical configurations.

Many complex phenomena, not captured by the previously mentioned models, affect the dynamic response of SFDs such as the inertia, the cavitation, the air entrainment, and complex geometrical features.

In the derivation of the Reynolds equation the presence of inertia is usually neglected. However, for large clearances and amplitudes of motions and frequencies, the dynamic pressurization of the lubricant film generates an added mass that was experimentally found in [7] to be of the same order of magnitude of the mass of the whole SFD. Many authors deal with the effect of inertia. In [8], assume that for moderate values of the Squeeze Reynolds Number ($Re = \frac{\rho \omega c l^2}{\mu} \leq 10$ with ρ being the density and μ being viscosity of the fluid, cl the SFD clearance and ω the vibration frequency) the fluid inertia does not affect the shape of the purely viscous velocity profile. Only the effect of temporal inertia is considered by the authors while both the effects of temporal and convective inertia are considered in [9].

Moreover, the presence of cavitation is considered as the main reason why predictions made with the simplified modes used in [1, 3] do not agree well with the experimental results. Zeidan and Vance in [10] report five different cavitation regimes: absence of cavitation, cavitation bubble following the journal, mixture of oil and air, vapor cavitation, combination of vapor and gaseous cavitation. The second cavitation regime may be assumed as a transient condition, present only at small whirling frequencies that

eventually turns into the third one at higher speeds. The most common regimes that are encountered are the third and the fourth that sometimes appear together as combined. In [11], Diaz and San Andrés focused on air ingestion and vapor cavitation. A SFD was tested by the authors in open-ends and in fully flooded configuration, considering different whirling frequencies and pressures of supply oil. The dynamic pression generated was measured in time and the differences between the two cavitation regimes was shown. When vapor cavitation occurs, the measured pressure evolution did not change for the different revolutions while, for air entrainment, the pressure profiles changed significantly from one revolution to the other. The differences showed by the two cavitation regimes often pushed the authors to treat and model them separately. The π-film model, also known as Gumbel condition, can be considered to model the vapor cavitation. In this case, the pressure is considered zero in the region where it assumes negative values. Half of the circumferential length of the SFD is therefore characterized by a ruptured lubricant film, see **Fig. 2**. More refined cavitation algorithms are the *Elrod's cavitation algorithm*, [12] and the *Linear Complementarity Problem* (LCP).
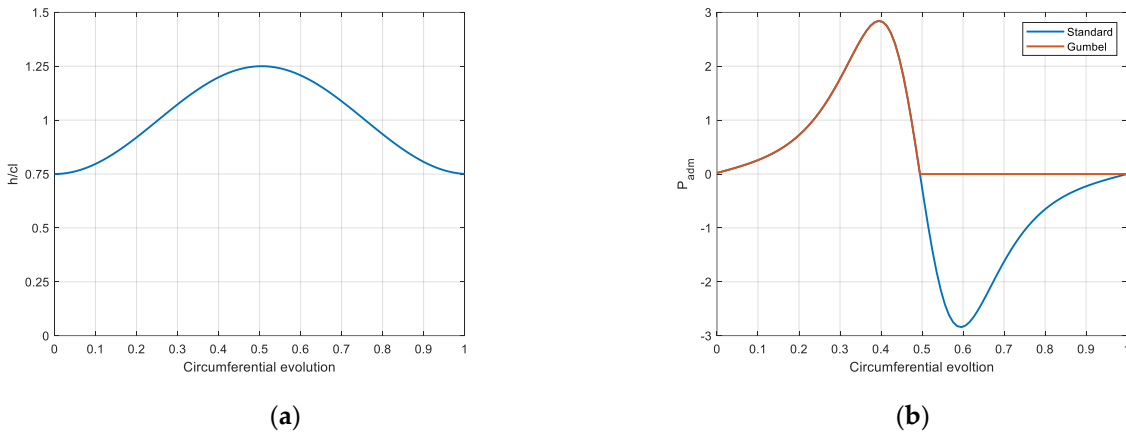

(a)   (b)

Fig. 2. Evolution of oil film thickness (**a**) and representation of Gumbel condition for vapor cavitation (**b**).

For what regards air ingestion, in [11], [13], and [14] its effect is experimentally investigated. When this phenomenon occurs, air is "sucked" inside the SFD, and, after some time, a fine mixture of oil and air bubbles is formed. Air bubbles are present also in the high-pressure zone and the variability of the values of the pressure peaks shown in [11] can be explained by their presence. Diaz [15] presented a detailed strategy, supported by numerous experimental results, to model the effect of the air entrainment in the 2-D Reynolds equation. The oil-air bubbly mixture is considered to be homogeneous and the distribution of the air content inside the mixture is calculated starting from a reference value. In the experimental campaign conducted in [13], and [14], the SFD is directly fed by a controlled mixture of oil and air. On the contrary, in industrial applications, pure oil is fed to the SFD, and air enters from the region where the lubricant is discharged. So, it is necessary to estimate the value of reference air ingested. A model to predict the air entrainment for short open-ends SFDs is presented in [16]. Mendez

then adapted the model of Diaz et al. [17] to finite length SFDs. Both models presented in [16] and [17] are based on the static form of the Rayleigh-Plesset equation to model the effect of air bubbles in the oil for open-ends SFDs. A more complex modeling strategy, where the complete form of the Rayleigh-Plesset equation is adopted, is presented by Gehannin et al. in [18]. Moreover, the differences between the modeling with the complete and the simplified form of the Rayleigh-Plesset equation are shown by the same authors.

A thorough experimental and numerical investigation on the effect of different geometrical configurations on the dynamic characteristics of SFDs is shown in [19]. The effect on the force coefficients of the SFD clearance, length, hole feeding and groove feeding, number and disposition of feeding holes, open ends and sealing ends, whirl orbit amplitude, and shape of orbit is investigated.

A model based on the 2D Reynolds equation is briefly introduced and validated with experimental and numerical results present in the literature. Then, an unbalanced centrifugal compressor is considered to evaluate the reduction of the level of the vibration with the addition of a SFD to the system. The effectiveness of the application of the SFD in correcting the instability of the machine is also investigated. The authors are aware that more accurate models based on the bulk-flow equations [20], and computational fluid dynamics [21–24] are described in the literature. Both modeling strategies are characterized by higher precision of the results. Unfortunately, both the modeling and computational efforts are higher.

2   SFD model

The 2D Reynolds equation, discretized with the finite difference approach, is adopted in the model proposed. To the standard equation, two extra terms are added to model the ai ingestion and inertia.

2.1   Oil film modeling

The dynamic behavior of SFDs is studied considering circular orbit motions of the journal, whether centered (see **Fig. 3**) or not, or small perturbations around the equilibrium position. The model proposed is developed for circular orbits. However, the model can be easily adapted to deal with non-circular orbits and small motions around the

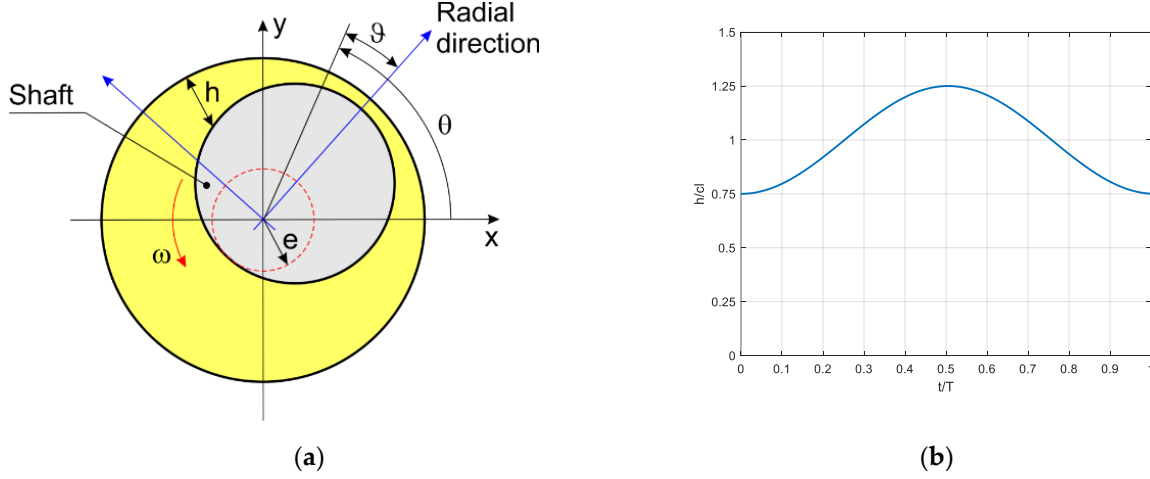equilibrium position when it is possible to describe the evolution of the lubricant film thickness in time.

(a)   (b)

Fig. 3. Representation of circular centered orbit (**a**) and relative evolution of oil film thickness (**b**)

The rotation ϑ in the relative frame of reference and the rotation θ in the absolute frame of reference (x-y) are related as follows:

$$\theta = \vartheta + \omega t \tag{1}$$

If the fixed reference system is considered, the variation in time and space domains of the oil film thickness can be written as:

$$h(\theta, t) = cl - (e \cos \omega t + e_s \cos \theta_s) \cos \theta - (e \sin \omega t + e_s \sin \theta_s) \sin \theta \tag{2}$$

where e_s and θ_s are the amplitude and phase of the static eccentricity. e is the orbit radius.

At each time instant:

$$\frac{\partial h}{\partial t} = -\omega \frac{\partial h}{\partial \vartheta} = -\omega \frac{\partial h}{\partial \theta} \tag{3}$$

Equation (3) allows to simplify the time derivatives in spatial derivatives if the orbiting frequency remains constant in time and if the feeding and sealing system are not considered. Therefore, the transformation proposed in equation (3) allows to reduce the calculation time since the pressure distribution at one orbit location is representative of the SFD behavior for the whole orbit.

2.2 Reynolds equation

The equations to describe the dynamic behavior of a viscous Newtonian fluid are the 3-D Navier-Stokes equations:

$$\frac{\partial \rho}{\partial t} + \nabla \cdot \left(\rho \vec{V} \right) = 0 \tag{4}$$

$$\rho \left(\frac{\partial \vec{V}}{\partial t} + \vec{V} \cdot \nabla(\vec{V}) \right) = -\nabla P + \nabla \cdot \left(\mu \nabla \vec{V} \right) + \nabla \left(-\frac{2\mu}{3} \nabla \cdot \vec{V} \right) + \rho g \tag{5}$$

Where (4) is the continuity equation and (5) are the conservation of momentum equations within the flow boundary.

For the SFD application, some simplifications can be considered. For example, fluid density ρ is considered constant, fluid kinematic viscosity is constant, inertia and body forces are neglected, fluid flow is considered laminar.

Since the fluid film thickness is small and the geometry of the SFD, the curvature of the surfaces can be neglected, and the surfaces can be considered planar. Moreover, the oil fil film thickness is about three orders of magnitudes lower than the axial and circumferential dimensions of the SFD sot the velocity gradients along the latter two dimensions are negligible. Finally:

$$\frac{\partial}{\partial x} \left(h^3 \frac{\partial P}{\partial x} \right) + \frac{\partial}{\partial z} \left(h^3 \frac{\partial P}{\partial z} \right) = 12\mu \frac{\partial}{\partial t} (h) \tag{6}$$

If the whirling frequency is constant, equation (3) can be substituted inside equation (6). On the other hand, if the effect of inertia is not neglected, the equations of momentum are different. In [25], the authors state that it is legitimate to hypothesize that the shape of the purely viscous velocity profiles is not affected by the fluid inertia, at least for moderate values of Reynolds number (Re). Moreover, considering average quantities in the flow equations the wall shear stress differences are approximated, [26].

In this work, a similar approach as in [26] is adopted. A single Reynolds-like equation is adopted in which the temporal inertia effect is added. Convective inertia effect is considered negligible as in [25]. In cylindrical coordinates:

$$\frac{\partial}{R\partial\theta} \left(\frac{h^3}{12\mu} \frac{\partial P}{R\partial\theta} \right) + \frac{\partial}{\partial y} \left(\frac{h^3}{12\mu} \frac{\partial P}{\partial y} \right) = \frac{\partial}{\partial t} (h) + \frac{Reh^2}{12\omega cl^2} \frac{\partial^2 h}{\partial t^2} \tag{7}$$

The comparison between the pressures, normalized w.r.t the reference ambient pressure, obtained with and without the inertial term is shown in **Fig. 4**. The pressure obtained considering the inertia term remains larger than the ambient reference for a longer time and is also flatter than the pressure calculated with the standard Reynolds equation. For the case with inertia, both the maximum and minimum values are reduced and slightly shifted. In this case the Reynolds number is about 3.5. From the classical Reynolds equation, the force obtained from the pressure distribution is purely tangential and opposes the vibration of the journal. On the other hand, if the temporal inertia term is considered, the resulting force is characterized both by a radial and tangential component. The first one counterbalance the radial acceleration introduced by the inertia term.
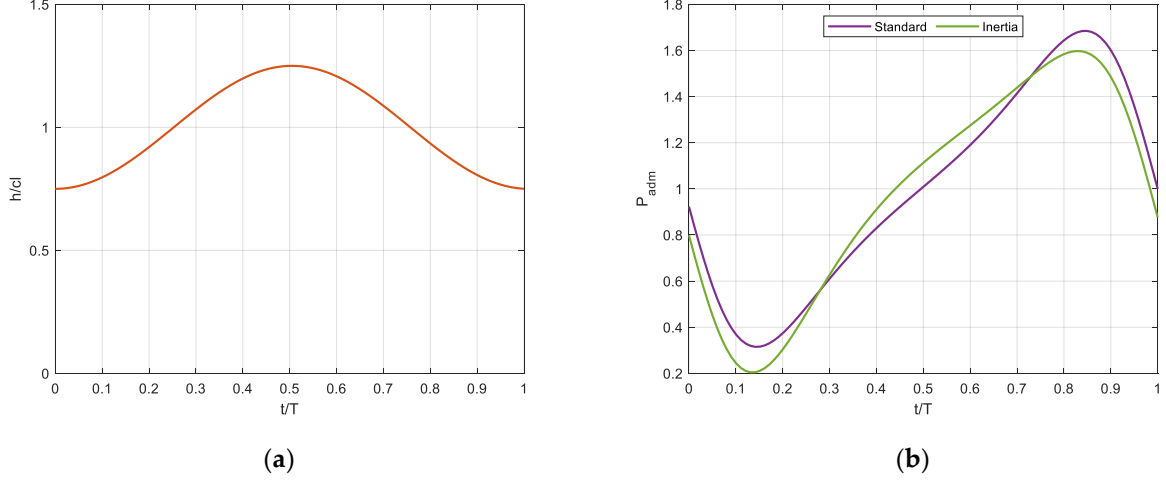
(a)

(b)

Fig. 4.(a) non-dimensional oil thickness; **(b)** non-dimensional pressure distribution for standard and Reynolds equation with inertia.

2.3 Air ingestion

Air entrainment is modeled considering the same approach introduced by the authors in [16]. The presence of the air bubbles in the lubricant affects the density and viscosity of the lubricant. The Reynolds equation becomes:

$$\frac{\partial}{R\,\partial\theta}\left(\frac{\rho h^3}{12\mu}\frac{\partial P}{R\partial\theta}\right) + \frac{\partial}{\partial z}\left(\frac{\rho h^3}{12\mu}\frac{\partial P}{\partial z}\right) = \frac{\partial}{\partial t}(\rho h) + \frac{Re h^2}{12\omega c^2}\frac{\partial^2 \rho h}{\partial t^2} \tag{8}$$

$$\rho = (1-\beta)\rho_L \tag{9}$$

$$\mu = (1-\beta)\mu_L \tag{10}$$

$$\beta = \frac{1}{1+\frac{P(x,t)-P_v}{P_{G\sigma}}(\frac{1}{\beta_0}-1)} \tag{11}$$

β is the air-mixture volume fraction, β_0 is the reference value for β, P_v is the vapor cavitation pressure, $P_{G\sigma}$ is the pressure of the air bubble for the critical radius, and μ_L and ρ_L are the viscosity and density for the pure oil.

The characterization of β_0 is necessary to evaluate the air entrainment level. A simplified model, based on the balance of the flow rates for short SFDs is presented in [16]. Unfortunately, the short bearing hypothesis is applicable only for $L/D < 0.2$. An approach valid for finite length SFD is introduced in [17]. The authors propose to estimate numerically the volumetric flowrate of air entering at the sides of the SFD to evaluate β_0. This approach is then repeated iteratively to update the dynamic pressure distribution until the convergence of the reference air-volume fraction. In this paper, the approach proposed in [17] is adopted.

2.4 Negative pressure zone

As previously mentioned, vapor cavitation can be modeled according to different algorithms. In this work, different cavitation models have been tested. Two are based on the LCP, [27] and [28], and one is based on the Elrod's cavitation algorithm, [29]. All the models tested are effective in calculating the pressure distribution when the standard Reynolds equation is considered. On the contrary, some difficulties were encountered when the inertia contribution is considered. The same holds for the modeling of the air ingestion.

Therefore, a simplified approach is adopted. The dynamic pressure is imposed to be equal to the vapor cavitation value when it assumes lower values than that threshold during the iterative solution of the Reynolds equation. As of now, this simplification allows the authors to include in the analysis some more interesting phenomena like the inertia effect and the air entrainment.

2.5 Geometry

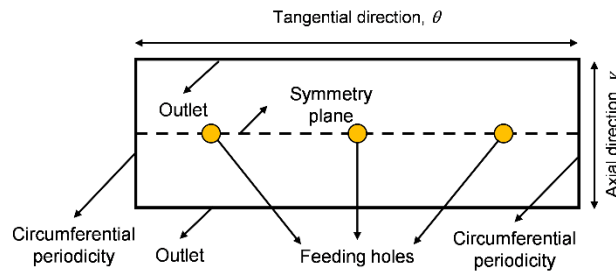The cylindrical geometry of the damper il opened in a bidimensional plane, see **Fig. 5**.

Fig. 5. 2D representation of the SFD.

The mesh considered for the spatial discretization is structured. The approach followed for the boundary conditions is presented in the sub-sections below.

2.6 Boundary Conditions

Inlet

The inlet boundary condition can be modeled in many ways. As a simplified approach, half of the SFD can be considered by applying the symmetry boundary condition:

$$\left.\frac{\partial P}{\partial y}\right|_{symmetry} = 0 \tag{12}$$

If equation (12) is adopted, the feeding system is not modeled.

On the contrary, if the feeding system is considered, the inlet flowrate is imposed at the orifices. Moreover, the hypothesis of laminar flow can be assumed to simplify the modeling. Then:

$$Q_{inlet} = C_i \left(P_{supply} - P(x_h, z_h) \right) \left[\frac{m^3}{s} \right]$$ (13)

where C_i is a coefficient that includes the orifice area and flow coefficient. $P(x_h, y_h)$ is the pressure of the oil at the hole location and P_{supply} is the feeding pressure far from the orifice. A more detailed description of the boundary condition can be found in [30].

In general, a backflow happens if $P_{supply} < P(x_h, z_h)$. Therefore, some oil exits the lands of the SFD and enters in the supply circuit. In practical applications check valves may be used to limit the effect of pressure waves in the supply circuit and to avoid backflows, [31]. In this case, if the oil pressure at the nodes of the holes is higher than the supply one, no boundary condition is assigned.

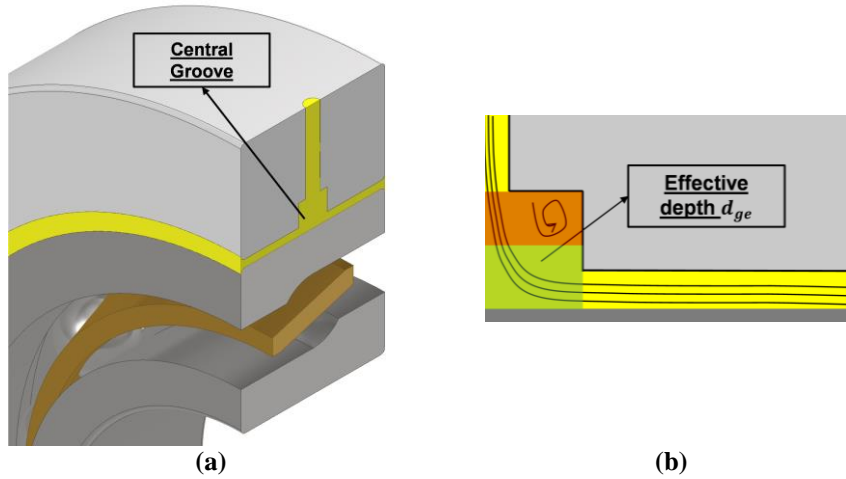Central grooves are often present in many applications as shown in **Fig. 6**.

(a)   (b)

Fig. 6. 3D representation of SFD with central groove (**a**); Schematization of the flow path passing through the central groove for half SFD (**b**).

In older literature, [30, 32], the authors suggest considering the groove as a region where the oil is at the feeding pressure. On the contrary, in [19] the authors report that large levels of dynamic pressure are registered in the groove, proving that the previous assumption was wrong. In this paper, the same approach introduced in [25] is adopted to model the effect of the central groove. The flow inside the groove is considered to be divided into two regions, a recirculating one and through-flow close to the journal, see **Fig. 6-b**. For the analysis, only the second one is considered effective in the generation of dynamic pressure in the groove. To evaluate the effective groove depth, in [25] the authors characterize experimentally the dynamic coefficients of the SFD. Then, the value of d_{ge} adopted in the model is tuned to obtain the same dynamic characteristics.

Outlet

Different approaches for the outlet boundary condition can be followed, see [5]. When the SFD ends are at ambient pressure the boundary condition is:

$$P(L,t) = P_{air} \qquad (14)$$

Where $P(L,t)$ is the pressure at the opening if the SFD. In this case the SFD is subjected to high air entrainment, which reduces the dynamic performance of the device. In case of pen ends configuration, larger inlet flow rate of oil is needed to compensate the oil that exits the damper. Therefore, seals are usually applied at the end. The sealing is usually partial to avoid an excessive oil heating that would decrease the SFD damping capacity. Among the various sealing mechanisms, the most common is the piston ring, [5, 31, 33].

The piston ring seal limits the outlet flow rate. It can be modeled as in [30]:

$$q_{out} = \frac{C_p(P(\theta,L) - P_{out})h_p^3}{12\mu w_p} \left[\frac{m^2}{s}\right] \qquad (15)$$

Where P_{out} is the pressure outside the seal, usually ambient pressure, C_p is the piston ring loss coefficient, $0 < C_p < 1$ and h_p is the piston ring radial gap and w_p is the axial dimension of the piston ring. The C_p coefficient strongly affects the sealing capability. Moreover, it may be difficult to correctly estimate its value. In this work, this coefficient will be considered as a tuning parameter. The authors are aware that the boundary conditions selected for this model represent a simplified approach. More complex and accurate formulations will be evaluated in the future developments.

Circumferential periodicity

The last boundary condition to be applied corresponds to the circumferential periodicity. To maintain the pressure continuity at the lateral sides of the geometry (**Fig. 5**), both the pressure and the circumferential pressure gradient along the axial direction must be equal on the two sides. To guarantee that it is sufficient to impose the pressures to be equal at both sides. The resulting circumferential pressure gradient respect the previous hypothesis.

2.7   Forces and Force Coefficients

The Reynolds equation is integrated once the geometry, the mesh, and the boundary conditions are assigned. Eventually the pressure distribution is obtained and is integrated along the circumferential and axial direction to obtain the forces acting on the shaft:

$$\begin{bmatrix} F_x \\ F_y \end{bmatrix} = -\int_0^L \int_0^{2\pi} P(\theta,z,t) \begin{bmatrix} \cos\theta \\ \sin\theta \end{bmatrix} R \, d\theta dy \qquad (16)$$

The tangential and radial forces, applied on the shaft in the point where the oil thickness is the minimum, can be calculated starting from the forces obtained in the x and y directions with a simple geometrical transformation.

The forces coefficients can be obtained once the forces are known. As reported in many sources, [6] and [19], no stiffness is generated by the damper itself. The damper forces are represented in linearized form:

$$\begin{bmatrix} F_x \\ F_y \end{bmatrix} = - \begin{bmatrix} C_{xx} & C_{xy} \\ C_{yx} & C_{yy} \end{bmatrix} \begin{bmatrix} v_x \\ v_y \end{bmatrix} - \begin{bmatrix} M_{xx} & M_{xy} \\ M_{yx} & M_{yy} \end{bmatrix} \begin{bmatrix} a_x \\ a_y \end{bmatrix} \tag{17}$$

Where v_x and v_y and a_x, a_y are the instantaneous journal velocities and accelerations, respectively.

Damping and added mass coefficients along the x and y directions are typical of small shaft displacement around the static equilibrium position. If circular centered orbits are considered, a constant rotating reaction film force is generated by the SFD. In most rotodynamic application, linearized force coefficients are considered. They represent the effect of infinitesimal amplitude motions about the equilibrium position on the bearing reaction forces. These coefficients can be adopted if the previously mentioned hypothesis is valid. However, in SFDs the orbit radius can be comparable to the clearance. The orbit described is far from being close to the equilibrium position. Therefore, the main hypothesis behind linearized force coefficients is violated and an alternative approach should be considered. An orbit-based model, as in [34], is adopted.

3   Model validation

Numerical and experimental results available in the literature have been considered for the model validation. In [19] the authors tested different geometrical configurations. Therefore, the results reported in [19] have been considered as a reference for this work. Three configurations (SFD B, E and F) have been selected for this paper. The differences among them are related to the clearance, length, presence of end seals and central groove. The diameter of the SFD is 127 mm. Moreover, the oil has density $\rho_L = 805 \ kg/m^3$ and viscosity $\mu_L = 26.5 \ mPa.s$ as in [19]. The characteristics of the SFDs considered for the validation are listed in **Table 1**.

Table 1. SFDs considered from [19]. d_G and L_G represent the physical depth and length of the central groove, not present in SFD E and F. d_E and L_E represent the depth and length of the grooves at the discharge, not present in SFD E and F. Piston ring seals are applied only for SFD B.

		SFD B	SFD E	SFD F
Length	$L\ [mm]$	2x 12.7	25.4	25.4
Clearance	$cl\ [mm]$	0.138	0.122	0.267
Central groove length	$L_G\ [mm$	12.5	no	no
Central groove depth	$d_G\ [mm]$	9.5	no	no
End groove length	$L_E\ [mm]$	2.5	no	no
End groove depth	$d_E\ [mm]$	3.5	no	no
Seal	-	yes	no	no

For SFD E and SFD F zero static eccentricity and variable orbit radius are considered. The e/cl ratios considered are 0.05, 0.14, 0.29, and 0.43. The tested frequencies are $10 \div 250\ Hz$ for SFD E and $10 \div 100\ Hz$ for SFD F. Since the force coefficients are constant for the selected frequency range, only their values at $100\ Hz$ and $50\ Hz$ are shown respectively. SFD B is instead tested in [19] considering a constant obit radius ($e = 0.055cl$) and for different values of static eccentricity. The frequency range considered is $110 - 210\ Hz$. Also, for this configuration, the force coefficients remain constant with the frequency. Therefore, the frequency considered for SFD B is $150\ Hz$. The effective groove depth of the model is tuned to match the force coefficients shown in [19]. The evolution of both the mass and damping coefficients for SFD F is shown in **Fig. 7** (**a**, **b**), for SFD E is shown in **Fig. 7** (**c**, **d**), and for SFD B is shown in **Fig. 7** (**e**, **f**). The results obtained with the current model and the results shown in [19] agree well with each other. For the three configurations, the damping coefficient shows a better agreement between the numerical and the experimental results. On the contrary, the agreement between the numerical and the experimental results for the mass coefficients is lower. This trend may be related to the high values of inlet pressure.
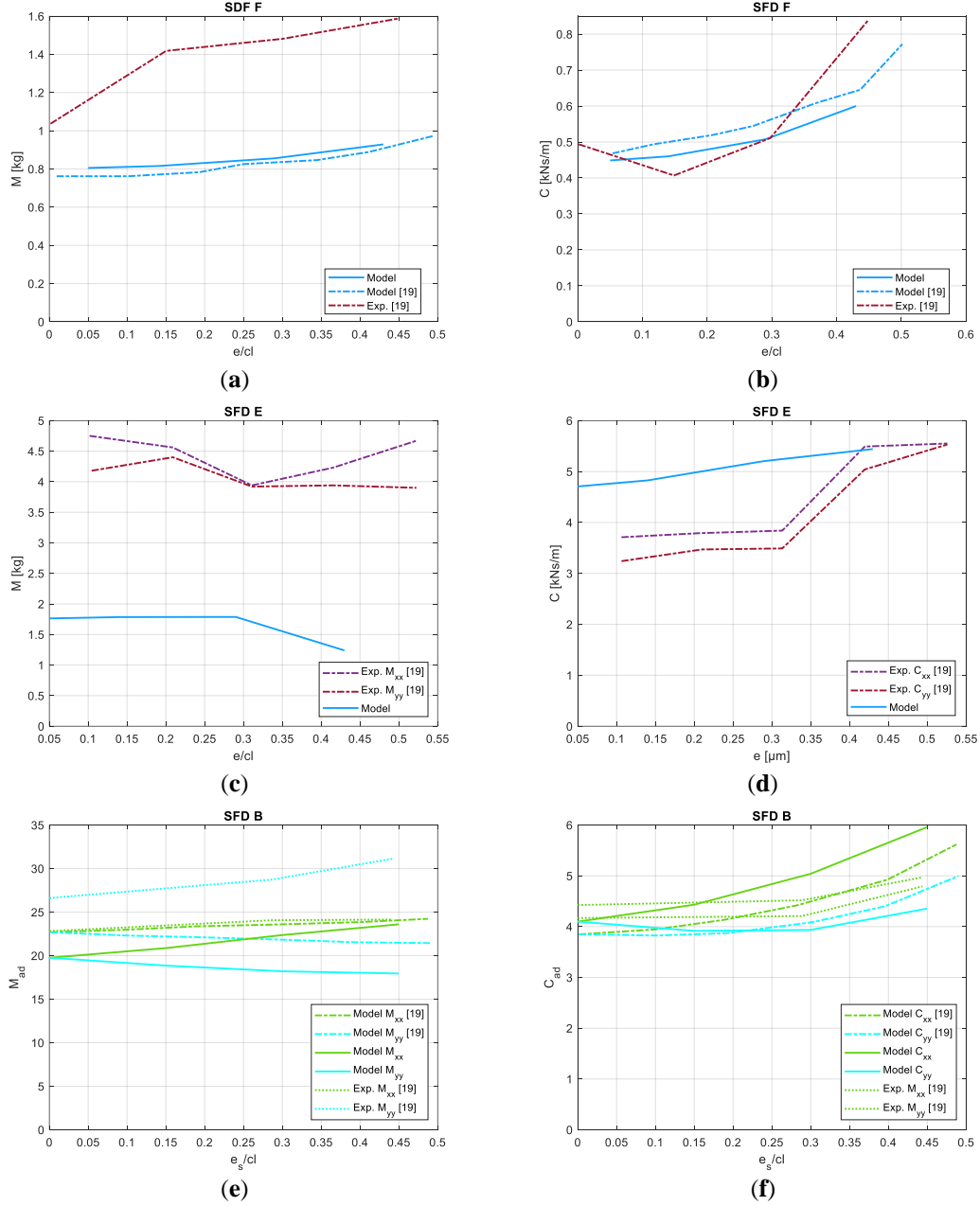
Fig. 7. SFD F: (**a**) evolution of mass coefficient as a function of the orbit radius, (**b**) evolution of damping coefficient as a function of the orbit radius. SFD E: (**c**) evolution of mass coefficient with orbit radius, (**d**) evolution of damping coefficient with orbit radius. SFD B open ends: (**e**) evolution of mass coefficient with static eccentricity, (**f**) evolution of damping coefficient with static eccentricity. Numerical and experimental results from [19].

4   Application

A finite beam analysis of a centrifugal compressor has been integrated with the proposed model. The shaft of the machine is $0.7\,m$ long and the nominal diameter is 50 mm. The impeller maximum diameter is 140 mm and the minimum one is 33 mm and the length is 70 mm. The finite element discretization of the structure, with a total of 34 nodes, is shown in **Fig. 8**.
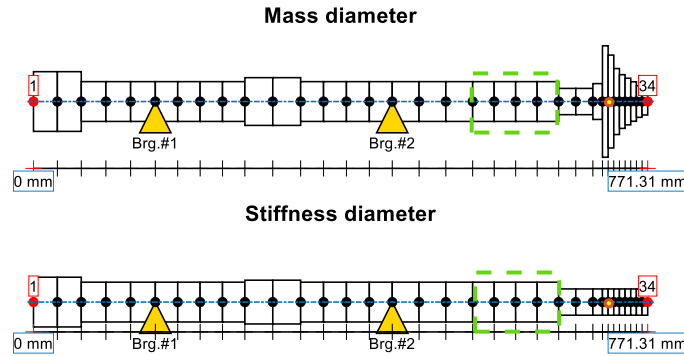

Fig. 8. Mass diameter and stiffness diameter FE discretization of the centrifugal compressor.

As shown in **Fig. 8**, the different elements are different in stiffness and mass diameter. The two roller element bearings supporting the machine are represented by the yellow triangles. Due to the characteristics of the bearings selected the system is barely damped. The sealing element is placed before the impeller and is indicated by the green rectangle. The presence of this component will be considered as the source of the instability. The reduction of the amplitude of the vibration and the mitigation of the instability are studied if the SFD is added to the system.

4.1   Vibration reduction

An unbalance force of $3 \times 10^{-6}\,[Kg \cdot m]$ is considered in the analysis at the yellow node of the impeller (node 27). For the vibration reduction analysis, the effect of the sealing element in the green rectangle is not taken into consideration. The focus is placed on the nodes of the impeller because, considering the tight clearances required to maximize the efficiency of the machine, an excessive level of the vibration could be harmful. The operational speed range considered for the compressor goes from $100 - 300\,Hz$. $200\,Hz$ is considered as the operating frequency. The forced response to the unbalance at node 27, 29, and 33 of the impeller is shown in **Fig. 9**. The amplitude of the vibration in the last node at $185\,Hz$, is close to $2 \times 10^{-4}\,m$. Large vibration amplitudes can compromise the safe operation of the compressor. Considerable damage can result from the contact between the stator and the rotor. For this reason, the level of the

vibration, both at the critical speed and at the operating speed, must be reduced as much as possible.
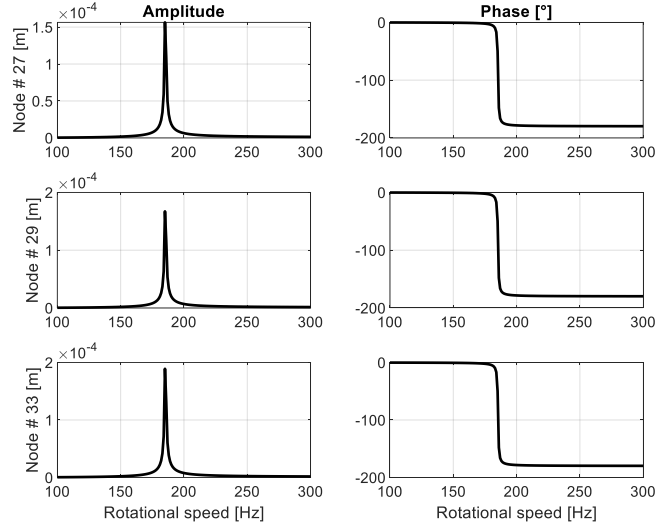

Fig. 9. Amplitude and phase of forced response at nodes 27, 29, and 33.

A SFD is applied in parallel with the bearing on the left to try to reduce the vibration peak. The new system is shown in **Fig. 10**. An external squirrel cage is supposed to be supporting the SFD. This component is defined by its own stiffness (k_{cage}) and mass (m_{cage}) respectively. An external source of added mass (m_{SFD}) and damping (c_{SFD}) are introduced by the SFD.
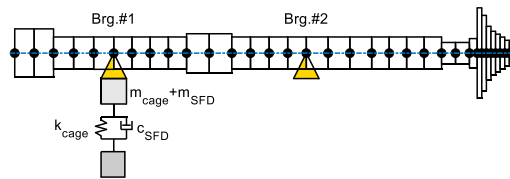

Fig. 10. System discretization with SFD.

A plain SFD without feeding system, seals, and grooves is considered. The characteristics of the SFD and the properties of the ISO VG 46 oil considered are listed in **Table 2**.

Table 2. Characteristics of the SFD and oil properties considered.

		SFD
Length	$L \; [mm]$	25
Clearance	$cl \; [mm]$	0.3
Diameter	$D \; [mm]$	100
Oil density	$\rho_L \; [Kg/m^3]$	870
Oil viscosity	$\mu_L \; [Pa \cdot s]$	0.0775

The forced response of the system when the squirrel cage is added to the system and when the SFD is applied is shown in **Fig. 11**. The effect that is obtained on the forced response of the system when the squirrel cage is added is the same as if a tuned mass damper is considered. The vibration peak is moved at a lower frequency, but the amplitude is not strongly affected. On the contrary, when the SFD dynamic effect is considered, the system is highly damped, and the amplitude of the vibration peak is strongly reduced.
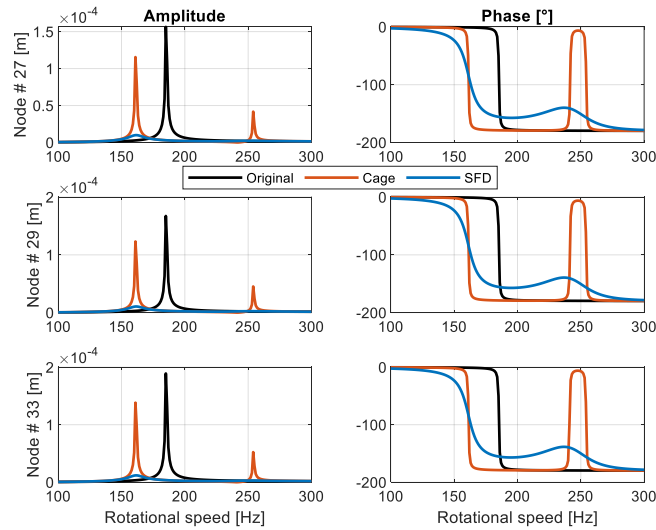
Fig. 11. Forced response comparison for original configuration, configuration with squirrel cage application and configuration with SFD.

To assess the effect of the SFD clearance on its dynamic characteristics, a parametric investigation has been performed. Considering different values of SFD clearance, the ratio between the peak of the force response at node 33 in the configuration with SFD and the original configuration without SFD, is shown in **Fig. 12**. If the ratio is lower than one, then the addition of the SFD determines a reduction of the vibration amplitude. The SFDs with the highest clearance minimize the forced response at the operating frequency. When the SFD clearance is $0.1 \; mm$, the amplitude of the vibration is almost identical as the one of the original configuration. The evolution of the force

coefficients of the SFD with the clearance is shown in **Fig. 13**. It is possible to appreciate that the reduction of the SFD clearance determines an increase in the force coefficients. However, the increase of the force coefficients does not determine a reduction of the vibration amplitude at the operation frequency considered for this application.
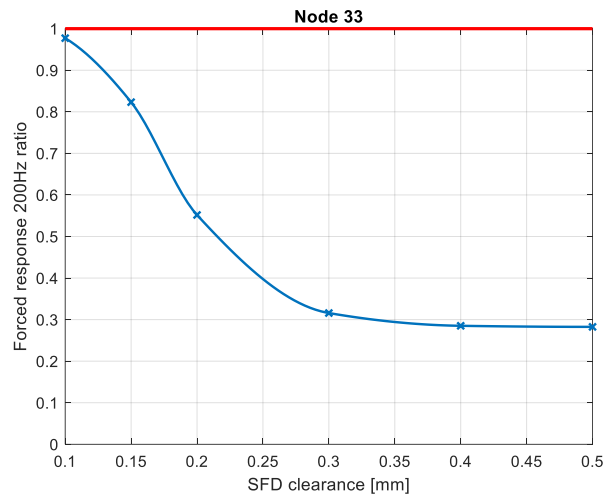
Fig. 12. Forced response peak ratio for different values of the SFD clearance.
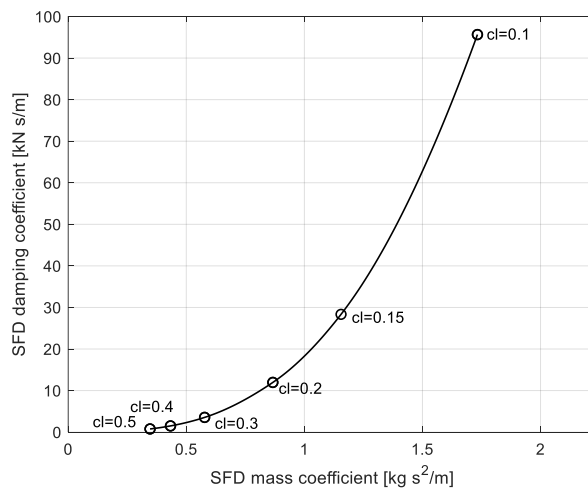
Fig. 13. Evolution of force coefficients at 200 Hz with the SFD clearance.

The evolution of the forced response at node 33 with the SFD clearance is shown in **Fig. 14**. The SFD that minimizes the forced response at $200\ Hz$ is not the one that guarantees the minimization of the first amplitude peak. Moreover, the SFD clearance seems to have no impact on the second peak around $250\ Hz$.
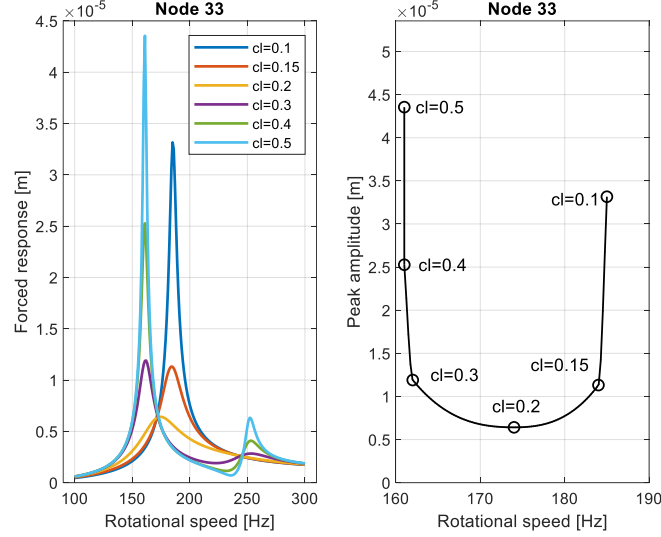
Fig. 14. Evolution of the forced response of the system at node 33 for the different SFD clearances considered and evolution of peak amplitude and first critical speed with SFD clearance.

The complexity of selecting the most appropriate SFD configuration is highlighted from this analysis. This decision is strongly dependent on the application that is considered. Moreover, the selection of the SFD configuration is strongly affected by the goal that must be obtained (peak minimization or amplitude reduction at operational frequency).

4.2 Correction of instability

In this section the effect of the seal placed before the impeller is considered as source of instability. The stiffness matrix at the nodes of the seal is introduced as follows:

$$K_{seal} = \begin{bmatrix} 0 & k_{seal} \\ -k_{seal} & 0 \end{bmatrix} \tag{18}$$

The value of k_{seal} is varied to establish when the sealing presence destabilizes the system resulting in positive values of the real parts of the eigenvalues of the system. The evolution of the maximum real part of the eigenvalues of the system with the increase of k_{seal} is shown in **Fig. 15**. The first instability is encountered at $k_{seal} = 15000\ N/m$. However, it is at $k_{seal} = 17500\ N/m$ that the system is unstable for the whole speed range. It is worth to notice that until $k_{seal} = 35000\ N/m$ only the real part of the first eigenvalue assumes positive values, for higher levels of k_{seal} also the real part of the fifth eigenvalue is positive.
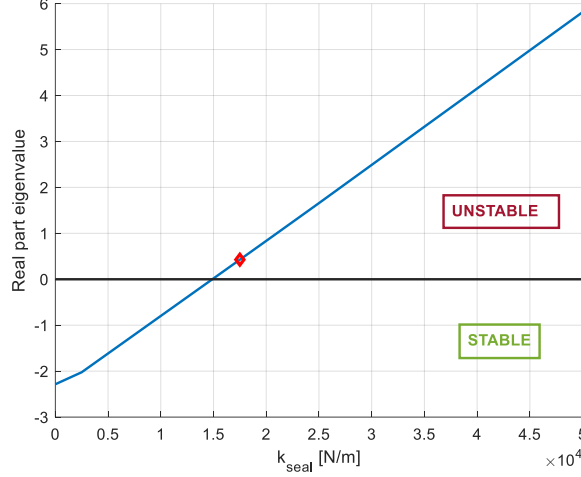
Fig. 15. Evolution of maximum real part of eigenvalues with k_{seal}.

For this analysis it is considered $k_{seal} = 17500 \; N/m$ since it is the first value at which the system is unstable for the whole speed range. To limit the instability, a SFD is applied in parallel with the first bearing as shown in **Fig. 10**. The addition of the SFD to the system will introduce damping that will counteract the presence of the instability. To study the stabilizing effect of the SFD, the evolution of the dimensionless damping factor with the speed is considered. This indicator is defined as follows:

$$\eta_i = -\frac{Real(\lambda_i)}{Imag(\lambda_i)} \tag{19}$$

where λ_i is the eigenvalue and η_i is the dimensionless damping factor for the i-th node. When η_i is positive the relative mode is unstable.

The tested SFD has the same characteristics of the one shown described in **Table 2** but the clearance is set to $0.5 \; mm$. The force coefficients obtained are like the one shown in **Fig. 13**. The evolution of the dimensionless damping factor for the original system and the SFD system for the unstable mode is shown in **Fig. 16**. As expected, for the original system, the dimensionless damping factor is negative for the whole speed range. The same holds for the configuration with the addition of the cage. On the contrary, the addition of the SFD can stabilize the system for the whole frequency range considered.

Then a parametric analysis on k_{seal} has been performed to investigate at which extent the application of the SFD is able to stabilize the system. The evolution of the dimensionless damping factor for different values of k_{seal} for the system with the SFD is shown in **Fig. 17**. For the SFD configuration considered the system is stabilized until $k_{seal} = 5e4 \; N/m$. In this case, also the 7th mode of the original system results unstable. On the contrary, when the SFD is applied, only the 1st mode is unstable. In case of higher values of k_{seal}, a different SFD configuration may guarantee the stability of the system.
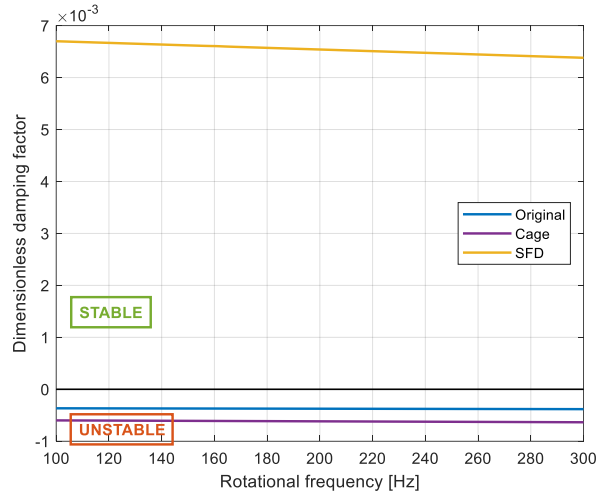
Fig. 16. Evolution of dimensionless damping factor for unstable modes of original, cage, and SFD system with rotational frequency.
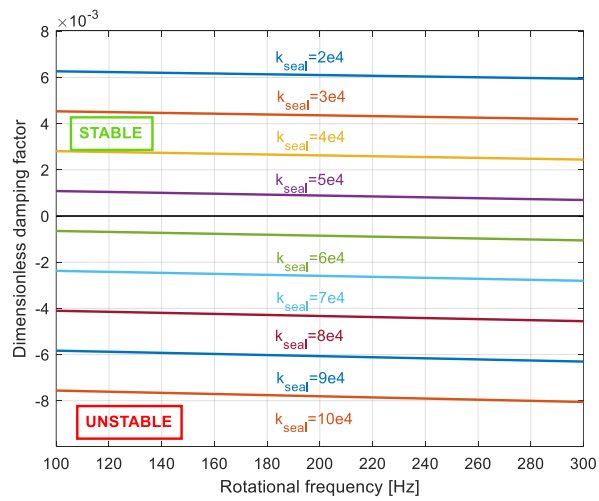

Fig. 17. Evolution of dimensionless damping factor for the unstable mode for different values of k_{seal} for the system with the SFD.

5   Conclusions

The state of the art on SFDs is investigated in this paper. The characteristic features of these components are highlighted and a review on the modeling strategies is given. A comprehensive model based on the 2D Reynolds equation is presented in the details.

The classical Reynolds equation is modified so to include the modeling of both the air entrainment and the temporal inertia.

The model is validated with both numerical and experimental results available in the literature. Then the model is integrated into a finite element code developed to study the dynamic response of turbomachines. The effectiveness of the SFD in the reduction of the level of the vibrations is investigated. From the results shown it is evident that the introduction of the SFD can drastically reduce the amplitude of the vibration. However, the optimal configuration to be selected strongly depends on the application considered and on the wanted effect. For example, it is shown that the optimal configuration to reduce the level of the vibration at a given frequency is not the same that minimize the amplitude of the vibration peak.

Secondly, the effectiveness of SFDs to mitigate the presence of destabilizing phenomena is investigated. The same turbomachine considered for the previous analysis is considered and the presence of a destabilizing sealing element is added. Different levels of source instability have been considered. The results obtained show that SFD are, in general, able to solve the presence of the instability. Also in this case, a trade-off may be needed when designing the SFD if both the vibration reduction and the instability correction are wanted.

The model proposed can be considered predict effectively and efficiently the dynamic behavior of SFDs. Moreover, it can be easily integrated in models used for the rotor dynamic analysis of turbomachines. The authors are aware that more accurate and precise models are present in the literature. However, some of them are more complex and require higher simulation time. An improvement in the modeling of the boundary conditions and in general in the modeling of the other characterizing aspects related to the SFDs may be required when studying more complex geometrical configurations.

References

1. Zeidan FY, San Andres L, Vance JM (1996) Design and Application of Squeeze Film Dampers in Rotating Machinery. In: Proceedings of the 25th Turbomachinery Symposium. Texas A&M University , pp 169–188

2. Vance JM, Zeidan FY, Murphy B (2010) Machinery Vibrations and Rotordynamics. John Wiley & Sons Inc.

3. Gunter Jr. EJ, Barrett LE, Allaire PE (1975) DESIGN AND APPLICATION OF SQUEEZE FILM DAMPERS FOR TURBOMACHINERY STABILIZATION. 127–141. https://doi.org/https://doi.org/10.21423/R1T37D

4. Chen WJ, Rajan M, Rajan SD, Nelson HD (1988) Optional Design of Squeeze Ilm Dampers for Flexible Rotor Systems. Journal of mechanisms, transmissions, and automation in design 110:166–174. https://doi.org/10.1115/1.3258922

5. della Pietra L, Adiletta G (2002) The squeeze film damper over four decades of investigations. Part I: Characteristics and operating features. Shock and Vibration Digest 34:3–26

6. San Andrés L (2012) Squeeze Film Damper: Operation, Models and Theoretical Issues. In: Modern Lubrication Theory. Texas A&M University

7. San Andrés L, Vance JM (1986) Effects of fluid inertia and turbulence on the force coefficients for squeeze film dampers. Journal of Engineering for Gas Turbines and Power 108:332–339. https://doi.org/10.1115/1.3239908

8. San Andrés LA, Vance JM (1987) Effects of fluid inertia on finite-length squeeze-film dampers. ASLE Transactions 30:384–393. https://doi.org/10.1080/05698198708981771

9. Hamzehlouia S, Behdinan K (2016) Squeeze Film Dampers Executing Small Amplitude Circular-Centered Orbits in High-Speed Turbomachinery. International Journal of Aerospace Engineering 2016:. https://doi.org/10.1155/2016/5127096

10. Zeidan FY, Vance JM (1990) Cavitation regimes in squeeze film dampers and their effect on the pressure distribution. Tribology Transactions 33:447–453. https://doi.org/10.1080/10402009008981975

11. Diaz SE, San Andrés LA (1999) Air entrainment vs. lubricant vaporization in Squeeze film dampers: An experimental assessment of their fundamental differences. In: Proceedings of the ASME Turbo Expo

12. Elrod HG (1981) Cavitation Algorithm. Journal of lubrication technology 103:350–354. https://doi.org/10.1115/1.3251669

13. Diaz SE, Andres LA (1999) Reduction of the dynamic load capacity in a squeeze film damper operating with a bubbly lubricants. Journal of Engineering for Gas Turbines and Power 121:703–709. https://doi.org/10.1115/1.2818530

14. San Andrés L, Diaz SE (2003) Flow visualization and forces from a squeeze film damper operating with natural air entrainment. Journal of Tribology 125:325–333. https://doi.org/10.1115/1.1510878

15. Diaz SE (1999) An engineering model for prediction of forces in SFD's and experimental validation for operation with entrainment. Texas A&M University

16. Diaz S, San Andrés L (2001) A model for squeeze film dampers operating with air entrainment and validation with experiments. Journal of Tribology 123:125–133. https://doi.org/10.1115/1.1330742

17. Méndez TH, Torres JE, Ciaccia MA, Díaz SE (2010) On the numerical prediction of finite length squeeze film dampers performance with free air entrainment. Journal of Engineering for Gas Turbines and Power 132:. https://doi.org/10.1115/1.2981182

18. Gehannin J, Arghir M, Bonneau O (2009) Evaluation of Rayleigh-Plesset equation based cavitation models for squeeze film dampers. Journal of Tribology 131:1–4. https://doi.org/10.1115/1.3063819

19. San Andrés L, Jeung S, Den S, Savela G (2016) Squeeze Film Dampers: An Experimental Appraisal of Their Dynamic Performance. In: Proceedings of Asia Turbomachinery Pump Symposium. Singapore

20. Gehannin J, Arghir M, Bonneau O (2010) Complete squeeze-film damper analysis based on the "Bulk Flow" equations. Tribology Transactions 53:84–96. https://doi.org/10.1080/10402000903226382

21. Xing C, Braun MJ, Li H (2009) A three-dimensional navier-stokes-based numerical model for squeeze-film dampers. Part 1-effects of gaseous cavitation on pressure distribution and damping coefficients without consideration of inertia. Tribology Transactions 52:680–694. https://doi.org/10.1080/10402000902913303

22. Xing C, Braun MJ, Li H (2009) A three-dimensional Navier-Stokes-based numerical model for squeeze film dampers. Part 2-effects of gaseous cavitation on the behavior of the squeeze film damper. Tribology Transactions 52:695–705. https://doi.org/10.1080/10402000902913311

23. Zhou H-L, Chen X, Zhang Y-Q, et al (2020) An analysis on the influence of air ingestion on vibration damping properties of squeeze film dampers. Tribology International 145:. https://doi.org/10.1016/j.triboint.2020.106168

24. Lee GJ, Kim J, Steen T (2017) Application of Computational Fluid Dynamics Simulation to Squeeze Film Damper Analysis. Journal of Engineering for Gas Turbines and Power 139:. https://doi.org/10.1115/1.4036511

25. Delgado A, San Andrés L (2010) A model for improved prediction of force coefficients in grooved squeeze film dampers and oil seal rings. Journal of Tribology 132:1–12. https://doi.org/10.1115/1.4001459

26. Fan T, Hamzehlouia S, Behdinan K (2017) The effect of lubricant inertia on fluid cavitation for high-speed squeeze film dampers. Journal of Vibroengineering 19:6122–6134. https://doi.org/10.21595/jve.2017.19314

27. Giacopini M, Fowell MT, Dini D, Strozzi A (2010) A mass-conserving complementarity formulation to study lubricant films in the presence of cavitation. Journal of Tribology 132:. https://doi.org/10.1115/1.4002215

28. Almqvist A, Fabricius J, Larsson R, Wall P (2014) A new approach for studying cavitation in lubrication. Journal of Tribology 136:. https://doi.org/10.1115/1.4025875

29. Hamzehlouia S, Behdinan K (2017) A study of lubricant inertia effects for squeeze film dampers incorporated into high-speed turbomachinery. Lubricants 5:. https://doi.org/10.3390/lubricants5040043

30. Marmol RA, Vance JM (1978) Squeeze film damper characteristics for gas turbine engines. Journal of Mechanical Design, Transactions of the ASME 100:139–146. https://doi.org/10.1115/1.3453878

31. San Andrés LS, Koo B, Jeung S-H (2019) Experimental Force Coefficients for Two Sealed Ends Squeeze Film Dampers (Piston Rings and O-Rings): An Assessment of Their Similarities and Differences. Journal of Engineering for Gas Turbines and Power 141:. https://doi.org/10.1115/1.4040902

32. Lund JW, Smalley AJ, Tecza AJ, Walton JF (1983) Squeeze-film damper technology: part 1 - prediction of finite length damper performance. https://doi.org/10.1115/83-gt-247

33. San Andrés L, Koo B (2019) Effect of lubricant supply pressure on SFD performance: Ends sealed with O-rings and piston rings

34. San Andrés L, Jeung S-H (2016) Orbit-Model Force Coefficients for Fluid Film Bearings: A Step beyond Linearization. Journal of Engineering for Gas Turbines and Power 138:. https://doi.org/10.1115/1.4031237